Article

Efficient encoding of aversive location by CA3 long-range projections

Graphical abstract

Highlights

- CA3 axons from intermediate to dorsal hippocampus encode aversive stimulus location

- During learning, new place-coding axons appear at the aversive stimulus location

- Late in learning, place coding shows enhanced stability

Authors

Negar Nikbakht, Martin Pofahl,
Albert Miguel-López, Fateme Kamali,
Tatjana Tchumatchenko, Heinz Beck

Correspondence

heinz.beck@ukbonn.de

In brief

Nikbakht et al. used *in vivo* imaging to examine how CA3 axons transfer affective information to the dorsal hippocampus for integration into spatial representations. CA3 axons projecting from the intermediate to dorsal hippocampus rapidly and robustly encode the location of an aversive experience via a defined sequence of changes in spatial coding.

CellPress

Article

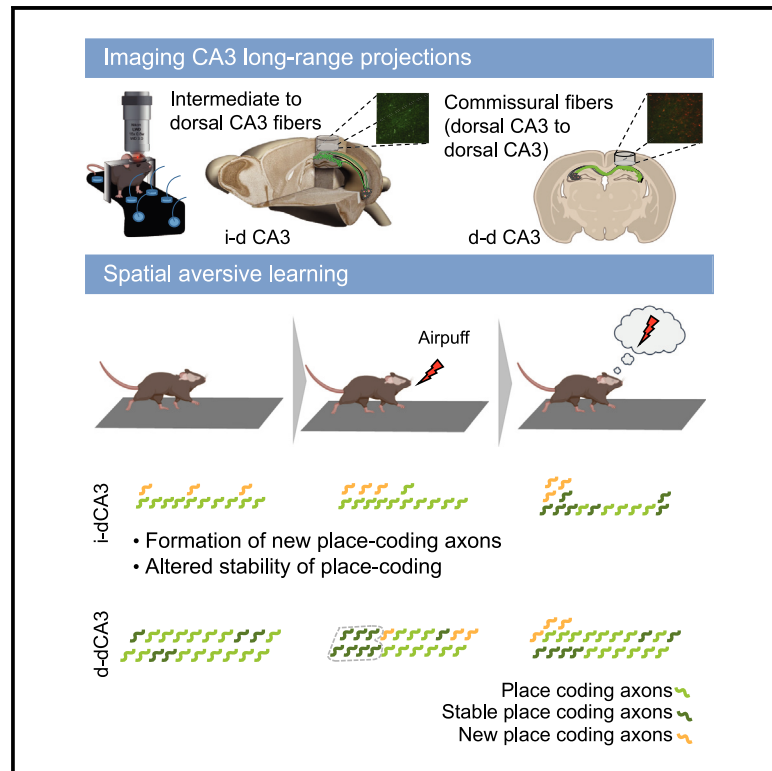# Efficient encoding of aversive location by CA3 long-range projections

Negar Nikbakht,[1,4] Martin Pofahl,[1,4] Albert Miguel-López,[1] Fateme Kamali,[1] Tatjana Tchumatchenko,[1,2] and Heinz Beck[1,2,3,5,*]

[1]University of Bonn, Medical Faculty, Institute for Experimental Epileptology and Cognition Research, Venusberg-Campus 1, 53127 Bonn, Germany
[2]University Hospital Bonn, Venusberg-Campus 1, 53127 Bonn, Germany
[3]Deutsches Zentrum für Neurodegenerative Erkrankungen e.V., Bonn, Germany
[4]These authors contributed equally
[5]Lead contact
*Correspondence: heinz.beck@ukbonn.de
https://doi.org/10.1016/j.celrep.2024.113957

SUMMARY

Memorizing locations that are harmful or dangerous is a key capability of all organisms and requires an integration of affective and spatial information. In mammals, the dorsal hippocampus mainly processes spatial information, while the intermediate to ventral hippocampal divisions receive affective information via the amygdala. However, how spatial and aversive information is integrated is currently unknown. To address this question, we recorded the activity of hippocampal long-range CA3 axons at single-axon resolution in mice forming an aversive spatial memory. We show that intermediate CA3 to dorsal CA3 (i-dCA3) projections rapidly overrepresent areas preceding the location of an aversive stimulus due to a spatially selective addition of new place-coding axons followed by spatially non-specific stabilization. This sequence significantly improves the encoding of location by the i-dCA3 axon population. These results suggest that i-dCA3 axons transmit a precise, denoised, and stable signal indicating imminent danger to the dorsal hippocampus.

INTRODUCTION

It is essential for animals and humans to memorize positions within an environment that can be harmful. Generating such memory maps requires an integration of spatial information with events of affective valence. The hippocampus processes both spatial and affective information, with the dorsal hippocampus being essential for spatial memory[1] while the ventral hippocampus underlies affective and stress-related behaviors.[2,3] Anatomical and functional evidence indicate that affective state signals reach the ventral hippocampus from principal neurons of the basolateral amygdala,[4] which project strongly to the ventral and intermediate, but not the dorsal, hippocampus.[5–7] However, it has remained unclear how such affective information in the ventral and intermediate hippocampus is conveyed to the dorsal hippocampus for integration with spatial information during memory formation.

CA3 pyramidal neurons are particularly interesting candidates for such information transfer, as they have been shown to form rich recurrent axon collaterals projecting for long distances along the septotemporal axis.[8–10] There is particularly rich connectivity within CA3 cells of the dorsal and intermediate hippocampus, with the ventral pole being relatively sparsely connected.[8,9,11,12] Longitudinal CA3 connectivity has been proposed to underlie longitudinal information transfer within the hippocampus, and disrupting this connection has effects on spatial memory forma-

tion.[13] However, it is currently an open question whether projections from the more ventral portions of CA3 to the dorsal CA3 are important for the integration of affective and spatial information during memory formation.

To assess the role of long-range CA3 projections in the association of aversive and spatial information, we followed the activity of individual CA3 axons over time using two-photon imaging. We then examined information transfer in CA3 axons projecting from the intermediate to dorsal hippocampus, as well as commissural CA3 axons, during formation of a memory associating an aversive stimulus with a specific location on a linear track.

RESULTS

Single-axon-resolution activity of CA3 projections

To assess which information is conveyed to dorsal CA3 from intermediate CA3, as well as between dorsal CA3 neurons, we performed chronic two-photon *in vivo* calcium imaging of activity in CA3 axons. We targeted CA3 neurons using viral gene transfer in an Et-iCre mouse line, which expresses Cre-recombinase in CA3 pyramidal neurons specifically (Figures S1A and S1B). We expressed GCaMP6s via virus injection in either the dorsal contralateral CA3 or the intermediate ipsilateral CA3 (Figures S1C and S1D) relative to the imaging site. This resulted in robust expression in commissural axons projecting between dorsal hippocampi (dorsal CA3 to dorsal CA3 [d-dCA3] axons)

or axons projecting from the ipsilateral ventro-intermediate to the dorsal hippocampus (intermediate CA3 to dorsal CA3 [i-dCA3] axons). Mice were habituated to run head fixed on a linear track under a two-photon microscope (Figures S2A–S2C; see Videos S1 and S2). The linear track was subdivided into three zones with distinct tactile cues (Figure S2A). To motivate mice to run, a reward was always given at the border of zones 3 and 1.

Two-photon imaging was carried out on three successive sessions on 2 consecutive days using the same cued belt (B_1–B_3; see STAR Methods) while imaging i-dCA3 axons (B_1 = 136, B_2 = 170, and B_3 = 181, Figures 1A and 1C), as well as commissural d-dCA3 axons (B_1 = 167, B_2 = 134, and B_3 = 119 axons, ; N = 4 mice for each axon category throughout the paper; Figures 1B and 1D; details of axon numbers are in Table S1). Single-axon activity in i-dCA3 and d-dCA3 axons was differently modulated by locomotion. We defined locomotion periods using a running speed threshold of >4 cm/s (see STAR Methods for further details). In i-dCA3 axons, locomotion was associated with decreased activity (1.6 ± 0.07 and 0.7 ± 0.11 Hz for immobility and locomotion, respectively; Wilcoxon rank-sum test: p = 1.47×10^{-29}, n = 181 axons, Figure 1E), while d-dCA3 axons, on average, increased activity during locomotion (1.2 ± 0.13 and 2.9 ± 0.17 Hz for immobility and locomotion, respectively, during B_1–B_3; Wilcoxon rank-sum test: p = 1.37×10^{-12}, n = 119, Figure 1F, left; for all three separate baseline trials B_1 to B_3, see Figure S2D). To quantify the locomotion-related behavior of single axons, we compared locomotion- vs. immobility-associated activity rates, revealing that numerous axons were virtually silent during either locomotion or immobility (Figures 1G, 1H, S2E, and S2F). For quantification, we arbitrarily defined axons as locomotion related or immobility related if the activity was 10-fold in one or the other condition. i-dCA3 axons more frequently showed dominant immobility-related activity than d-dCA3 axons (69.6% vs. 10.1% in i-dCA3 and d-dCA3 axons, $\chi2_{(2, 138)}$ = 109.8, p < 0.001), while dominant running-related activity was observed very rarely in i-dCA3 axons compared to d-dCA3 axons (2.8% vs. 24.36% in i-dCA3 and d-dCA3 axons, $\chi2_{(2, N = 34)}$ = 109.8, p < 0.001). Thus, i-dCA3 axons differ from d-dCA3 axons by a high fraction of cells that are mostly active during immobility.

Ventral and dorsal CA3 neurons are thought to encode spatial information differently.[14–16] Therefore, we asked whether this difference is reflected in their respective projections to dorsal CA3. We identified CA3 axons with significant spatial tuning using published criteria for place coding in imaging data[17] (see Figure S3 for examples and STAR Methods). In both i-dCA3 and d-dCA3 axons, the place fields tiled the entire extent of the linear track (Figures 1I, 1K, and S4A). Consistent with published data,[14–16] we found a significantly higher fraction of place-coding axons in d-dCA3 compared to i-dCA3 axons (73.3 vs. 23.0% on average in the baseline sessions, $\chi2$ test for $B_{1(1,473)}$ = 12.5, p = 3.6×10^{-4}, n = 122 and 48). The precision of each significantly place-coding axon was examined using tuning vector analysis[18] (which was calculated as the weighted mean of all running-related events in polar coordinates). The angle of the spatial tuning vector represents the linear track position where the peak activity occurs, and the length of the vector represents the spatial spread of events and hence the place field precision (Figure S3). Even though there were less place-coding axons in i-dCA3 compared

to d-dCA3, individual axon place-coding precision was comparable between these two groups during baseline sessions (Figure 1M, Mann-Whitney test, p = 0.99).

To assess a preference in place code across the axon population, we calculated an average place preference vector for each session from all individual spatial tuning vectors (Figures 1J and 1L, left). The place preference vector direction points to the linear track position on the track with the highest density of individual tuning vectors, and its length is a proxy for the density of tuning vectors around the preferred direction. During all baseline sessions, the vector length was close to zero. To address the significance of place preference across the axon populations, we tested the distribution of tuning vectors for uniformity (Figures 1J and 1L, right, Hermans-Rasson test, i-dCA3 B_1: p = 0.22, d-dCA3 B_1: p = 0.21; Figure S4B), which revealed no significant place preference in either projection in any baseline session.

Aversive spatial learning task

To examine how spatial representations in the two CA3 systems change during aversive learning, we developed a learning paradigm in which head-fixed mice learned the location of an aversive stimulus on a linear track. This allowed us to study how aversive information is encoded within an established spatial map. In a training phase, we introduced an aversive airpuff stimulation at the border of zones 1 and 2 on the linear track (Figure 2A, left). When the aversive stimulation was added, mice began to exhibit a brief reduction of speed within 10 cm before the aversive stimulus location in virtually all laps, albeit at slightly different locations (see representative heatmaps in Figure S5A and average speeds in Figure S5B). To quantify slowing, we used two approaches. First, we utilized a computer vision algorithm based on Hough transform to analyze the location where mice showed the most consistent slowing across all laps in a session and whether this location was significantly above chance level (Figure 2A, bottom right; see STAR Methods). This method delivers a slowing location in an unsupervised and unbiased manner. While slowing locations were randomly distributed on the linear track in the baseline trials (example shown for B_2 to B_3, not significant [n.s.] for null hypothesis test; see STAR Methods; n = 8 mice), mice systematically slowed down preceding the airpuff location during training. Training sessions continued until a last training session, T_n, when mice showed consistent slowing around the airpuff zone (examples shown for T_n). Following training, we carried out a probe (Pr) session without aversive airpuff stimulation in which we also observed consistent slowing around the airpuff location (Pr, p = 0.00006, Figure 2A, right). This shows that mice memorize the location of mild aversive stimuli on the linear track. In these analyses, we excluded the reward zone (± 10 cm around the reward site), where mice always showed consistent slowing. Additionally, we quantified where speed reductions larger than 1 SD of the speed profile during the session in all laps occurred on the linear track (see STAR Methods). In baseline sessions, ~1/3 of speed reductions occurred in the linear track section (zone 1) preceding the airpuff location. During training and Pr sessions, speed reductions were significantly more frequent in the zone preceding the airpuff location (Figure S5C). Thus, both analyses indicate that mice learn the location of the aversive stimulus.
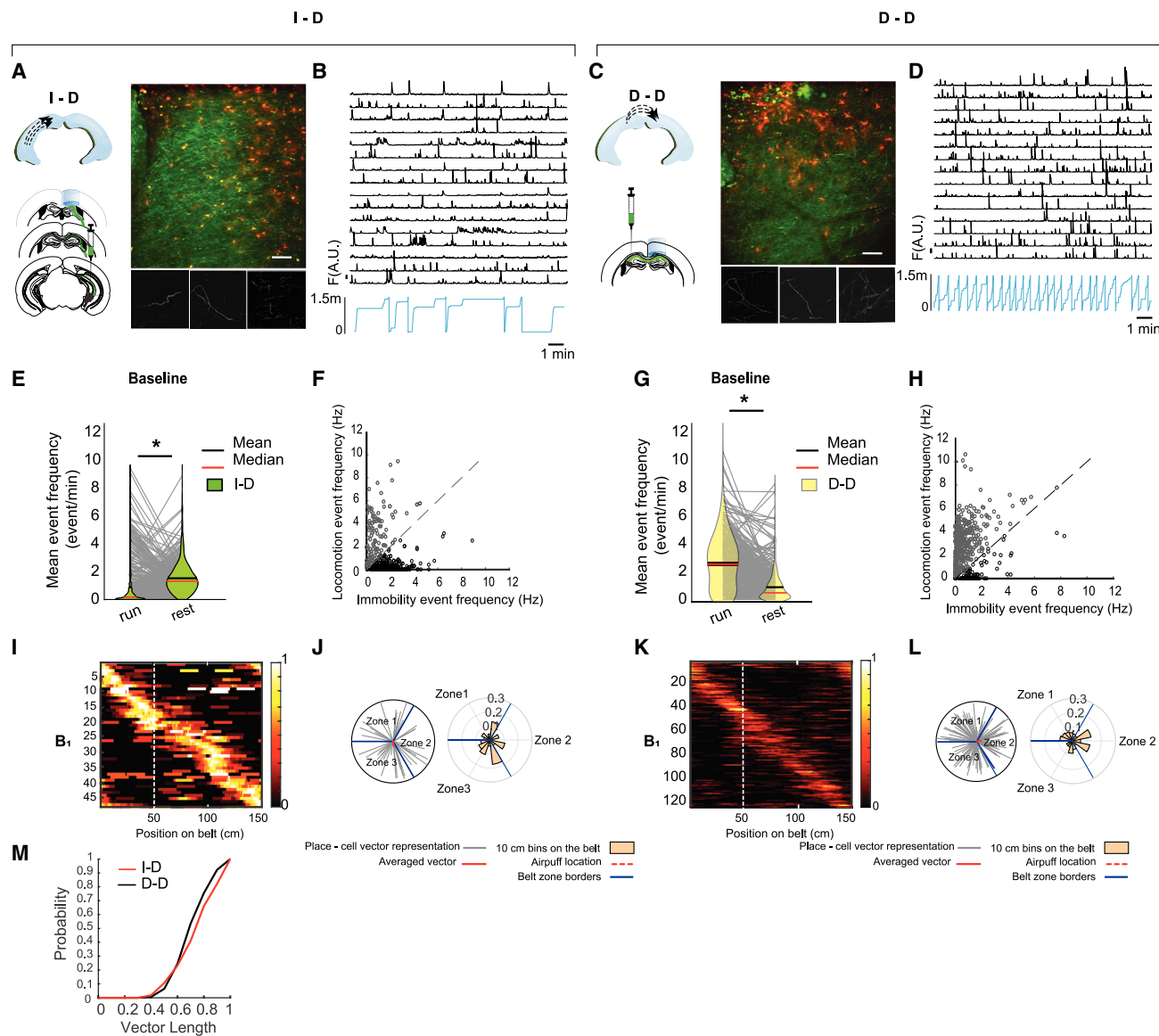
Figure 1. Spatial coding in i-dCA3 and d-dCA3 axons

(A and C) Strategy for expression of GCaMP6 and *in vivo* two-photon imaging for axons projecting from intermediate to dorsal hippocampus (i-dCA3 axons; A) and axons projecting between dorsal hippocampi (d-dCA3 axons; C). Average projection images of the imaging site shows G-CaMP6 expressed in CA3 axons emanating from ipsilateral intermediate CA3 (for i-dCA3) and dorsal contralateral CA3 (for d-dCA3) hippocampi (green) and mCherry expressed in astrocytes as fiducial marker (red). Scale bars: 100 μm. Cranial window position is indicated in light blue. Position of GCaMP viral gene transfer with AAV is indicated by green syringe. Rightmost images indicate representative fields of view for two-photon imaging, with examples of individual axon segments separated by non-negative matrix factorization shown in the insets.

(B and D) Activity of a representative subset of i-dCA3 (B) and d-dCA3 (D) axon segments. Blue indicates the mouse position on the linear track.

(E and G) Average rates of events detected in i-dCA3 (E; N = 4 mice, n = 487 axons) and d-dCA3 (G; N = 4 mice, n = 420 axons) axons during locomotion (run) and immobility (rest).

(F and H) Relation of activity during locomotion and immobility plotted for each individual axon in the i-dCA3 (F) and d-dCA3 (H) axon populations. Gray indicates cells that are more active during locomotion and black the opposite.

(I and K) Normalized place maps calculated with the onsets of Ca^{2+} events for the first baseline session (B_1, N = 4 mice).

(J and L) Polar plot representation of all place-coding axons for i-dCA3 (N = 4 mice, n = 48 axons) and d-dCA3 (N = 4 mice, n = 121 axons) axons for the first baseline session. Each gray line represents the position of mean activity, and the length represents peak normalized activity at that position for each individual axon. Average place preference vectors from all axons in a given session are represented by dense black lines. Circular histograms summarizing the place preference are shown on the right of each polar plot. Asterisks indicate significance in the Hermans-Rasson test.

(M) Average vector length of i-dCA3 and d-dCA3 axons during baseline sessions B_1–B_3.
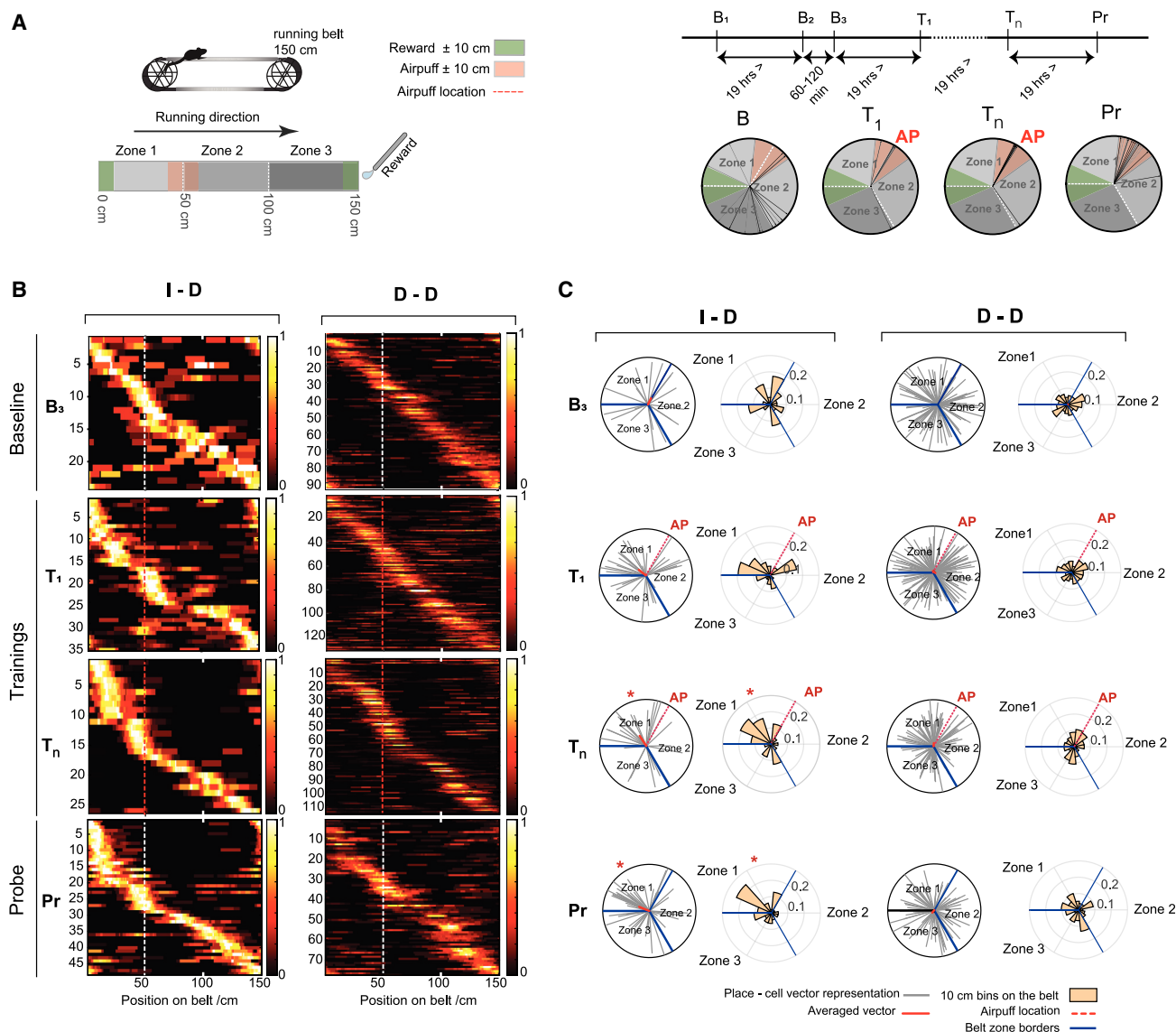
Figure 2. Spatial coding in i-dCA3 and d-dCA3 axons during learning

(A) Left: schematic of the linear track. The 150 cm belt had three zones, with rewards delivered at zone transition 3-1 (green shading ±10 cm around transition), aversive stimulations only during training delivered at zone transition 1-2 (red shading ±10 cm around transition), and one neutral zone transition (2-3). Top right: schematic depicting the behavioral protocol in which animals learn the location of an aversive airpuff stimulus on a linear track. T_1 designates the first training session after baseline sessions B_1–B_3 and T_n the last training sessions before the probe (Pr) (see STAR Methods). Bottom right: evaluation of consistent slowing on the linear track by applying a Hough transform to the running speed data (see STAR Methods). Images show circular representations of the linear track. Red: zone ±10 cm around the airpuff location. Green: zone ±10 cm around the reward location. The location of preferential slowing is indicated by radial lines in the circular representations for each session (each line corresponds to one mouse, N = 8 mice). We show as indicated baseline sessions (B_1–B_2), first and last training sessions (T_1, T_n), and Pr trial without aversive airpuff stimulation (Pr).

(B) Normalized place maps calculated with the onsets of Ca^{2+} for the last baseline session (B_3), the first (T_1) and last training sessions (T_n), and the Pr session (Pr) for i-dCA3 and d-dCA3 axons as indicated (number of place-coding axons is indicated on the y axis and in Table S1).

(C) Polar plot representation of all place-coding axons for i-dCA3 (N = 4 mice) and d-dCA3 (N = 4 mice) axons (number of place-coding axons is indicated in the maps). Each gray line represents one axon, with the direction representing the position of peak activity and the length representing peak normalized activity at that position. Summed vectors from all axons in a given session are represented by dense black lines. Circular histograms summarizing the place preference are shown on the right of each polar plot. Asterisks indicate significance in the Hermans-Rasson test.

Changed spatial representations in i-dCA3 and d-dCA3 axons during learning

We then examined how spatial representations in i-dCA3 and d-dCA3 axons change during learning. In i-dCA3 axons, the frac-

tion of place-coding axons increased (omnibus test over all sessions: $\chi^2_{(3, 688)} = 9.8$, p = 0.02, post-test for difference to B_3 with Bonferroni correction: B_3-Pr, p = 0.002, Figure S6A; see Table S2A). In d-dCA3 axons, the fraction of place-coding axons

remained at similar levels throughout learning with no significant changes compared to the baseline condition (omnibus test over all sessions: $\chi2_{(3, 541)} = 7.8$, $p = 0.05$, post-test with Bonferroni correction, n.s., Figure S6A; Table S2B). On an individual-axon level, the place-coding precision assessed by each spatial tuning vector length did not significantly change during learning in either d-d or i-dCA3 axons (Figures S6B and S6C, Kruskall-Wallis test, $p = 0.99$ and 0.99 for d-d and i-dCA3 axons, respectively).

Looking at the spatial distribution of place fields in i-dCA3 axons, we found that, in contrast to d-dCA3 axons, the linear track segment preceding the airpuff location became increasingly more represented during training trials (see Figure 2B, left). These changes were maintained during the Pr trial (Pr in Figure 2B). This was further reflected in the circular distribution of the i-dCA3 tuning vectors, which was non-uniform in the last training and Pr sessions (Figure 2C, Hermans-Rasson test, B_3: $p = 0.74$, T_1: $p = 0.06$, $T_n = 0.009$, Pr: $p = 0.004$).[19] This non-uniformity is reflected in the properties of the average place preference vector computed as a sum of all place vectors of place-coding i-dCA3 and d-dCA3 axons, respectively. The average vector length increased (Figure S6D) and pointed toward the zone preceding the airpuff (Figure S6E).

As running speed can have an influence on location-related activity, we examined if spatially selective changes observed in place coding of i-dCA3 axons could be accounted for by training-induced slowing of the mice. Several lines of evidence indicate that this is not the case. Firstly, we examined if place representations are generally correlated or anticorrelated to running speed during baseline trials. For this correlation, we first quantified the density of place fields by averaging all place fields of each projection. This distribution showed spatial variation in both projections (Figure S4C, shown in red). We then examined if anticorrelations exist between running speed and place field density (Figure S4C, shown in blue and red, respectively). During all baseline sessions, there was a significant anticorrelation of running speed and place fields for d-dCA3 axon populations, while this was not the case for the i-dCA3 axon population (see Figure S6G; Table S6). Thus, slowing is unlikely to contribute strongly to increased place representations in i-dCA3 but could potentially do so in d-dCA3 axon populations. Over training, an anticorrelation developed in i-dCA3 axon populations. This is expected because, after training, there is a strong increase in place-related activity in the pre-airpuff area, where there is also slowing. In d-dCA3 axons, anticorrelations are maintained throughout training (see Figure S6G; Table S6).

Secondly, we also find no significant anticorrelations when specifically considering changes in speed and place field density at the specific reward- and aversive-related locations for i-dCA3 axon populations, whereas they are present for d-dCA3 axon populations, consistent with the above findings (detailed analysis in Figures S7F and S7G).

A third, final line of evidence that suggests that the modification in spatial coding cannot be due only to slowing is based on the comparison to the reward site, at which slowing also takes place. We observed slowing at the reward site in all sessions to an extent that was similar to the slowing observed at the pre-airpuff zone after training (see detailed analysis in Figures S7A–

S7E). Yet, no modification or preference of place representation is seen in this area in either i-d or d-dCA3 axons during the baseline or later sessions (see Figures 2B and 2C). This specificity also indicates that a general effect of slowing cannot account for the changes in place-related activity in i-dCA3 axons.

Overall, therefore, these data suggest that i-dCA3 spatial maps incorporate new spatial information during learning of the aversive stimulus location.

Addition of newly place-coding axons is spatially selective

To address the question of how individual axons synthesize altered spatial maps, we tracked individual axons across sessions (see STAR Methods and Figure S8; Table S3A) and analyzed changes in spatial representations of single axons between pairs of sessions. We studied transitions during the baseline condition (B_1-B_2), the beginning of training transition from the last baseline to training (B_3-T_1), the entire training phase (B_3-T_n), or the memory maintenance phase (T_n-Pr; see Figure 3A). We chose these session pairs because they encompass identical time intervals.

We first studied newly place-coding axons, defined as axons that did not exhibit significant spatial coding in the first session and subsequently converted to place coding (example shown in Figure 3B). The overall fraction of newly place-coding axons expressed as a fraction of the tracked axons did not significantly change in either i-dCA3 axons (Figure 3C, omnibus test $\chi2_{(3, 70)} = 11.16$, $p = 0.026$, post-test n.s.; see Table S3B) or d-dCA3 axons (Figure 3C, omnibus test $\chi2_{(3, 172)} = 9.4$, $p = 0.3$; see Table S3C). However, we observed that newly place-coding i-dCA3 axons preferably encoded locations within the pre-airpuff zone. In the i-dCA3 projection, during both learning (B_3-T_n) and memory maintenance (T_n-Pr), newly place-coding axons appeared with a spatial preference either within or at the border of the pre-airpuff zone (Figure 3D, Hermans-Rasson test, $p = 0.003$ and 0.003, respectively). In contrast, newly place-coding d-dCA3 axons did not show a spatial preference during learning trials. However, new d-dCA3 axons exhibited a spatial preference during memory maintenance (T_n-Pr), almost completely sparing the post-airpuff zone of the linear track (zone 2, Figure 3D, Hermans-Rasson test, $p = 0.028$; see Figure S9A for polar plots and statistics of all sessions). This spatial preference was also apparent when looking at the average place preference vector of all place vectors for newly place-coding axons. In this case, the direction of the summed vector during training moved toward the pre-airpuff zone (Figure 3E, right, gray shading indicates the pre-airpuff zone).

Stabilization of place-coding axons

Selective stabilization of neuronal ensembles has also been proposed to be important to integrate salient information into spatial maps.[20,21] We studied the same session pairs as above (B_1-B_2, B_3-T_1, B_3-T_n, and T_n-Pr; Figure 2A) and first quantified the fraction of axons showing significant place coding in both sessions (recurring axon; see example in Figure 2F). At late stages of learning, there was a pronounced increase in the fraction of recurring axons in i-dCA3, but not d-dCA3, axons (Figure 2G, omnibus $\chi2$ test for i-dCA3 $\chi2_{(3, N = 70)} = 11.04$, $p = 0.026$, asterisk shows significance of comparison to B_1-B_2 transition,
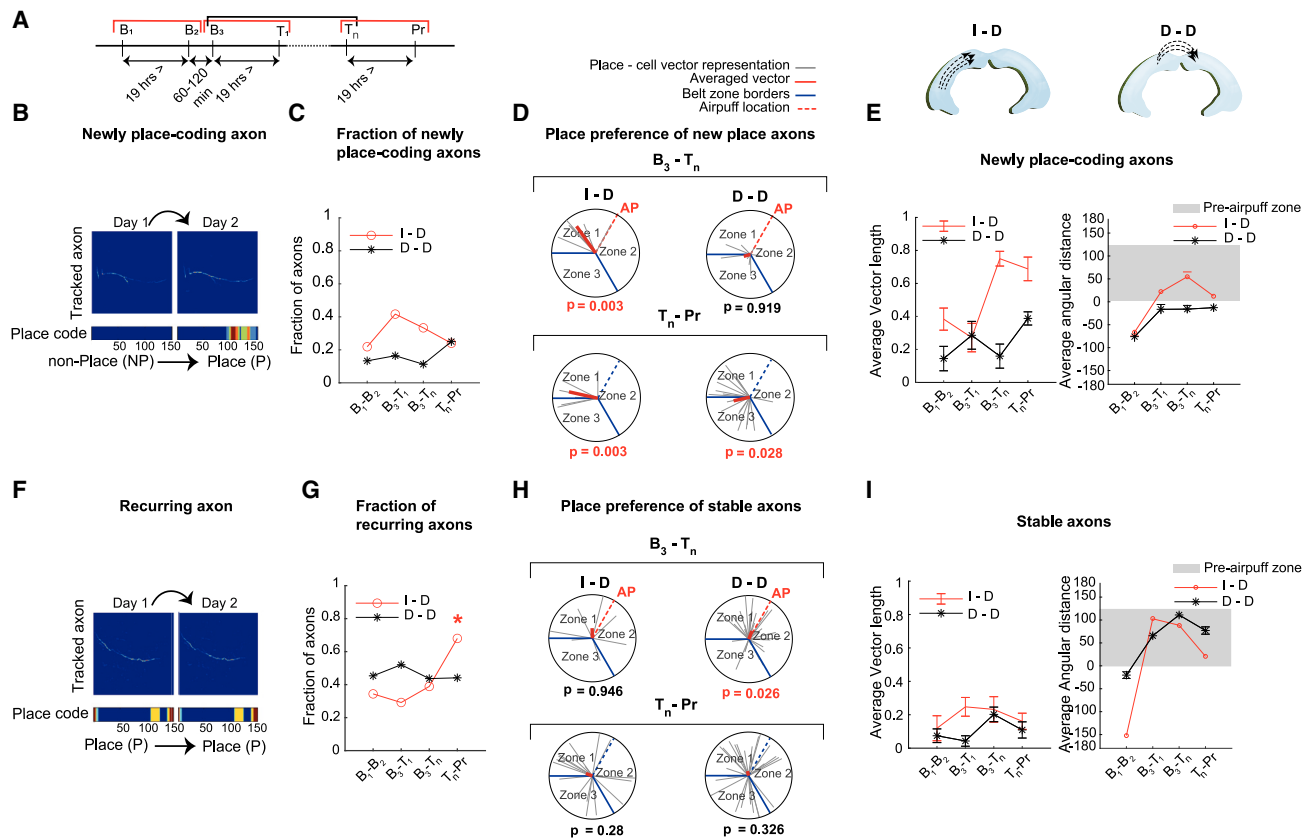
Figure 3. Spatially selective newly place-coding axons appear during learning

(A) Schematic of analyzed session pairs B_1-B_2, B_3-T_1, B_3-T_n, and T_n-Pr.

(B) Example of a newly place-coding axon that did not exhibit significant spatial selectivity in the previous session but started coding the space in the current session.

(C) Changes in the fraction of newly place-coding axons throughout learning in i-dCA3 (red) and d-dCA3 (black) axons.

(D) Radial plots with vector representations of the place preference of all newly place-coding axons (i-dCA3, N = 4, n = 6 for B_3-T_n and n = 6 for T_n-Pr; d-dCA3, N = 4, n = 8 for B_3-T_n and n = 17 for T_n-Pr). The vector direction represents the position of peak activity in T_n, and the length of the vector represents peak normalized ΔF/F. Red line indicates the summed vector. See Figure S6 for polar plots and statistics of all sessions.

(E) Average vector length (left) and direction of the summed vector (right) of all place vectors for *de novo* axons. Gray shading indicates the pre-airpuff zone.

(F) Example of a stably place-coding axon that exhibits significant spatial selectivity in two consecutive sessions.

(G) Fraction of stable place-coding i-dCA3 (red) and d-dCA3 (black) axons. Asterisk indicates significance, χ2 test (see Tables S3 and S4 for more details).

(H) Radial plots with vector representations of the place preference of stably place-coding axons (i-dCA3, N = 4, n = 7 for B_3-T_n and n = 17 for T_n-Pr; d-dCA3, N = 4, n = 31 for B_3-T_n and n = 30 for T_n-Pr). See Figure S8 for polar plots and statistics of all sessions. As in (D), the vector direction represents the position of peak activity, and the length of the vector represents peak normalized ΔF/F, in this case in the second of two sessions.

(I) Average vector length (left) and direction of the summed vector (right) of all place vectors for recurrent place-coding axons during the second of the two sessions indicated. Gray shading indicates the pre-airpuff zone.

χ2 test, Bonferroni-adjusted p = 0.042; see Table S3B for full statistical results). The amount of remapping, measured as the shift of the location at which peak place-related activity was observed, did not change during learning in either i-dCA3 or d-dCA3 stable axon populations (Figure S9C).

We then studied if recurrently place-coding axons might occur with a preferential spatial location. We represented the spatial tuning of each recurrent axon in the second of the two sessions with a vector in a polar plot (Figure 3H; see Figure S9B for all sessions). This allowed us to assess if recurrent axons occur in a spatially selective manner. We could not find such spatial specificity in i-dCA3 axons in any of the session pairs (Figures 3G and S9B), not even during memory maintenance, where a signif-

icant increase in stability was seen (see Figure 3G). In d-dCA3 axons, we identified a spatially specific increase in stability only during late learning (B_3-T_n session pair, Hermans-Rasson test, p = 0.026). Most recurrently place-coding axons encoded the pre-airpuff zone (Figure 3I, right). We note that d-dCA3 axon place coding is inversely correlated with running speed (see Figures S6F and S6G; Table S6); thus, it is possible that slowing in the pre-airpuff zone contributes to this increased spatial representation. When we analyzed how the summed vector of all recurring place axons changes during learning, we found that its direction moved toward the pre-airpuff zone in both i-dCA3 and d-dCA3 axon populations (Figure 3I, right, gray shading indicates the pre-airpuff zone), perhaps arguing
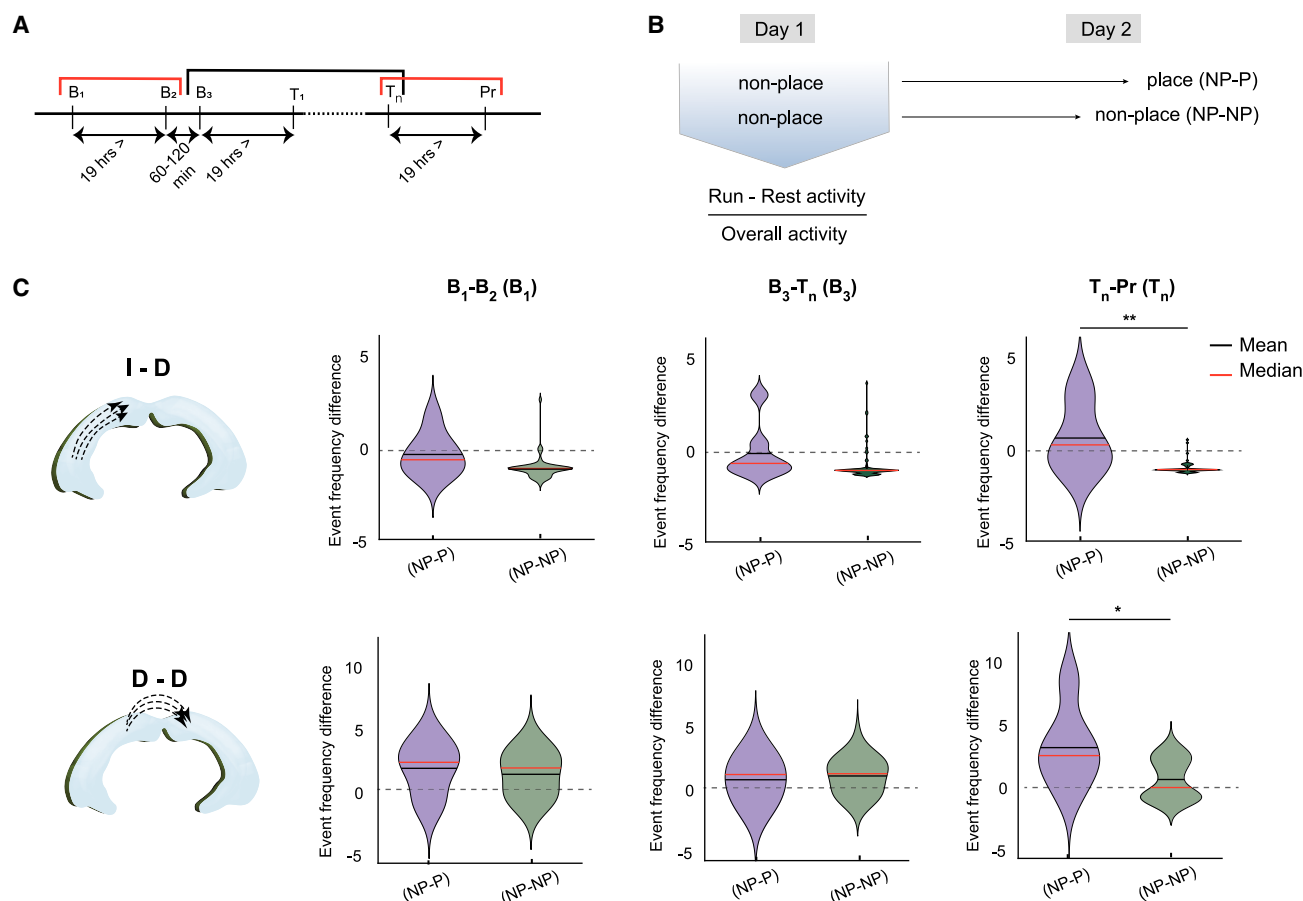
Figure 4. Properties of i-dCA3 and d-dCA3 axons prior to incorporation into spatial codes

(A) Schematic of analyzed session pairs B_1-B_2 (total tracked axons: i-dCA3 n = 83, N = 4 mice; d-dCA3, n = 85, N = 4 mice), B_3-T_1 (total tracked axons: i-dCA3 n = 121, N = 4 mice; d-dCA3, n = 78, N = 4 mice), B_3-T_n (total tracked axons: i-dCA3 n = 87, N = 4 mice; d-dCA3, n = 82, N = 4 mice), and T_n-Pr (total tracked axons: i-dCA3 n = 82, N = 4 mice; d-dCA3, n = 70, N = 4 mice).

(B) Schematic of the axon groups analyzed (NP-NP: non-place axons that remain non-place axons; NP-P: axons that convert from non-place coding to place coding). During the first session, a ratio indicating the relationship of activity during locomotion and immobility was calculated (zero if activities are equal and positive if activity during locomotion is larger than during immobility).

(C) Activity difference during run and rest in i-dCA3 and d-dCA3 axons comparing NP-P and NP-NP categories. Asterisks indicate significance, Kruskal-Wallis test, ** = 0.0004 for i-dCA3 and * = 0.01 for d-dCA3. For full statistics, see Table S4; for detailed rendering of data for all sessions, see Figure S10.

for a subtler increased representation of the pre-airpuff location when considering the entire place cell population.

Properties of i-dCA3 and d-dCA3 axons that are newly incorporated into spatial codes

The data so far reveal that i-dCA3 axons form a new place code resulting in an increased representation of the linear track area preceding the aversive stimulation during learning. We found that most i-dCA3 neurons are virtually silent during locomotion but are active during immobility (see Figure 1). This raises the question of if i-dCA3 axons destined to become place axons are also silent during locomotion or if they become more active in the preceding session. We therefore quantified the normalized difference between running and immobility during the first of two sessions and separated non-place axons that remain non-place axons from those that are non-place axons but convert to place axons (Figures 4A and 4B). In i-dCA3 axons, non-place axons

were more active in the cases where they subsequently became place axons when compared to non-place axons that remained non-place coding (Figure 4C, top). Such a phenomenon was not observed in d-dCA3 axons, in which non-place-coding axons were significantly more active than i-dCA3 axons irrespective of their subsequent fate (Figure 4C, cf. top and bottom; Table S4; Figure S10). In all sessions, as expected, place-coding axons had significantly higher locomotion-related activity than both other categories of neurons (data not shown; Table S4). These results show that the transition to place coding is preceded by a transition of i-dCA3 cells from the population of preferentially rest-active neurons to more locomotion-related activity.

Changed spatial population codes in i-dCA3 axons during learning

Finally, we asked if the changes in spatial representation described so far result in altered or improved spatial population
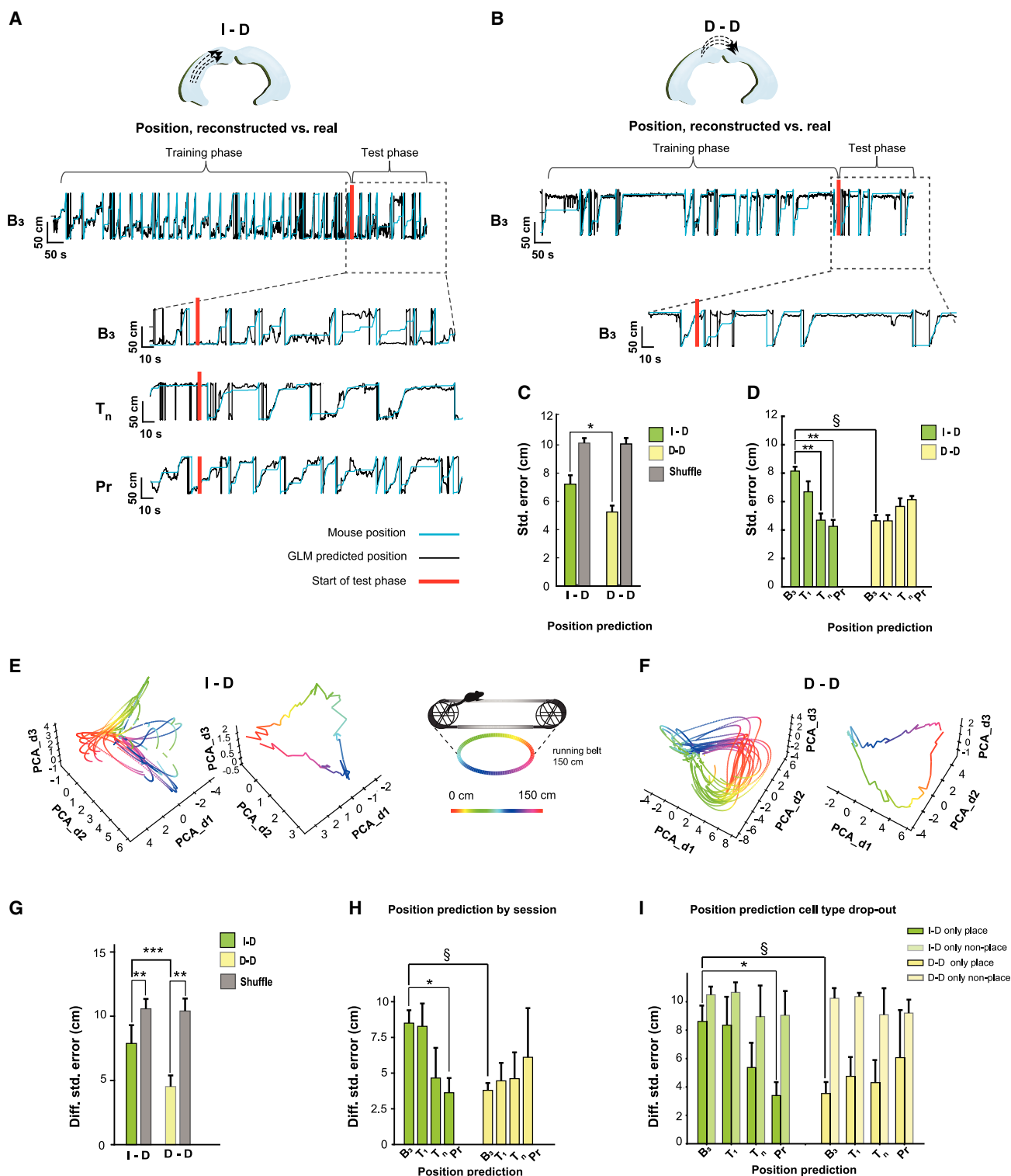
Figure 5. Altered population coding of space in i-dCA3 axons during learning

(A and B) Examples for the application of a generalized linear model (GLM) to predict the location of mice on the linear track from i-dCA3 (C; sessions B_3, T_n, and Pr shown) and d-dCA3 activity (D; session B_3 shown). Insets depict magnifications of the last 5 min of the session used to assess GLM performance (transition point to testing indicated by red line) after training during the first 15 min of the session. The GLM prediction of mouse location is shown in blue and the actual location in black in all images.

(legend continued on next page)

codes during spatial aversive learning. To determine how i-dCA3 and d-dCA3 axons encode space at the population level before and after learning, we used a generalized linear model (GLM; see STAR Methods) (Figures 5A and 5B). The GLM was trained on the first 16 min of the session, and the performance was assessed during the last 4 min (see insets in Figures 5A and 5B). The prediction of the GLM was tested against a prediction obtained with shuffled data (see STAR Methods). Both the d-dCA3 axon population and the i-dCA3 axon population predicted location significantly better than shuffled data in all sessions (Figure 5C, unpaired t test, $p < 0.05$, pooled data from B_1–B_3 shown). During learning, there were systematic changes in the prediction of position in both axon systems. Two-way ANOVA revealed significant changes across sessions ($F_{(1.507,9.041)} = 5.402$, $p < 0.035$) and a significant interaction of axon identity and time ($F_{(3,18)} = p < 0.0001$). Consistently, post-tests revealed that under baseline conditions, d-dCA3 axons were significantly better predictors of position compared to i-dCA3 axons (session B_3, Sidak's post-test, $p = 0.0026$, § in Figure 5D; see also Figure 5C, sessions B_1–B_3, $p < 0.05$, unpaired t test), consistent with the higher number of place-coding axons. However, the i-dCA3 axon populations got significantly better during training in encoding the animals' position (Dunnett's post-test for i-dCA3 group B_3 vs. T_n: $p = 0.0098$ and B_3 vs. Pr: $p = 0.0012$, ** in Figure 5D), reaching levels comparable to d-dCA3 axons.

As a second approach to assess spatial population codes, we performed principal-component analysis (PCA; see STAR Methods). The neuronal state captured by the first three components (Figures 5E and 5F, example for a baseline session B_3, colors indicate the location on the linear track) showed that PCA trajectories relate smoothly to the position on the linear track in both axon populations. We used the PCA components explaining 90% of the variance (see STAR Methods) to predict the position of mice on the linear track with similar precision to the GLM and also with better prediction compared to shuffled data (unpaired t test, $p < 0.005$ for baseline comparisons and $p < 0.0005$ for shuffled vs. non-shuffled, pooled data from B_1–B_3 shown, Figure 5G). PCA-based position prediction also revealed progressively improved position encoding during learning in i-dCA3 axons, while position encoding of d-dCA3 axons was not enhanced. Two-way ANOVA showed significant interaction

of axon identity and time ($F_{(3,18)} = p = 0.0035$; Dunnett's post-test for i-dCA3 group B_3 vs. Pr: $p = 0.0043$, * in Figure 5H). Consistently, post-tests revealed that under baseline conditions, d-dCA3 axons were significantly better predictors of position compared to i-dCA3 axons (session B_3, Sidak's post-test, $p = 0.0028$, § in Figure 5H). In ventral CA3[16] as well as dorsal DG and CA1,[22] both place- and non-place-coding neurons can contribute to a distributed representation of space.

We therefore asked how much place-coding i-dCA3 axons contribute to the position prediction as well as the improved position prediction. Overall, place-coding axons contribute more to the position prediction compared to non-place-coding axons (Figure S11). Across learning, we then systematically predicted position using non-place and place-coding axons, respectively. This revealed that i-dCA3 place-coding axons were the major contributors to the improved spatial prediction (Figure 5I) even though they constitute a minority of the entire axon population. This could be due to the fact that in i-dCA3 axon populations, the non-place-coding axon population shows very little activity during locomotion (see Table S5; see also Figure 3), and thus the main activity in this axon population is highly related to place without ancillary noise.

These results collectively suggest that i-dCA3 axons generate a sparse but information-rich code carrying information about aversive location to the dorsal hippocampus.

DISCUSSION

We have shown how CA3 axons transfer affective information to the dorsal hippocampus for integration into spatial representations. We found that CA3 axons projecting from the intermediate to dorsal hippocampus rapidly and robustly encode the space correlated with aversive experience. During learning, new place-coding axons appear and are integrated during the memory maintenance phase into a new spatial map that is subsequently stabilized. We showed that CA3 commissural axons show spatially selective stabilization during learning and later also exhibit spatially selective appearance of newly place-coding axons during memory maintenance. To show this, we have tracked neuronal activity in CA3 longitudinal projections from the intermediate to dorsal hippocampus at single-axon resolution during formation of a spatial aversive memory.

(C) Prediction of the GLM for i-dCA3 and d-dCA3 axon populations in sessions B_1–B_3 tested against shuffled data (gray bars). Asterisks indicate significance $p < 0.05$, unpaired t test.

(D) Position prediction of the GLM for i-dCA3 (green) and d-dCA3 (yellow) axons across learning. § indicates Sidak's post-test, ** indicate Dunnett's post-test, ** = 0.0098 for B_3 vs. T_n and ** = 0.0012 for B_3 vs. Pr.

(E) Example for PCA of population activity in i-dCA3 axon populations. The PCA plots show the individual laps on the belt (left) as well as a depiction of trajectories in PCA space averaged across laps (right). The first three PCA components are depicted for a baseline session, B_3. The color code reflects the mouse position on the belt (see schematic).

(F) As in (E) but for d-dCA3 axon population.

(G) PCA-based decoding of mouse location for i-dCA3 and d-dCA3 axon populations in sessions B_1–B_3 tested against shuffled data (gray bars). Asterisks indicate significance $p < 0.05$, unpaired t test.

(H) PCA-based decoding of mouse location during learning in i-dCA3 and d-dCA3 axons. § indicates Sidak's post-test, * indicates Dunnett's post-test, * = 0.0043 for B_3 vs. Pr. I. PCA-based decoding of mouse location during learning is based on only non-place-coding or only place-coding i-dCA3 or d-dCA3 axons. Two-way ANOVA shows a significant interaction of axon identity and time ($F_{(3,18)} = 6.53$, $p = 0.003$). § indicates Sidak's post-test, $p = 0.008$ for i-dCA3 B_3 vs. d-dCA3 B_3 and * indicates Dunnett's post-test significance = 0.0105, p value for place only vs. non-place only in i-dCA3 for Pr = 0.018. Two-way ANOVA reveals a significant effect of place only vs. non-place only in the d-dCA3 group of $p = 0.0018$, Sidak's post-test for place only vs. non-place only, $p = 0.0012$ and $p = 0.015$ for B_3 and T_1, respectively.
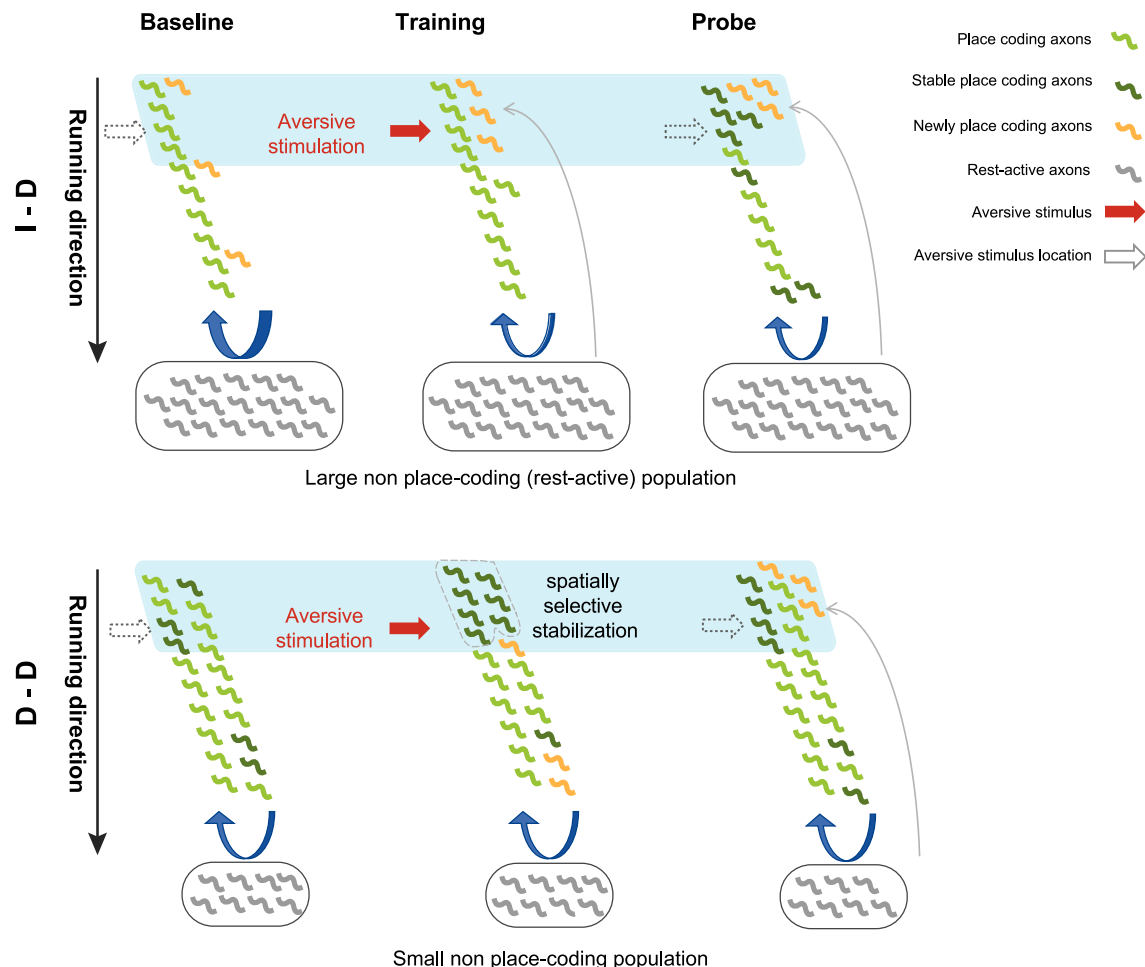
Figure 6. Sequence of changes in i-dCA3 and d-dCA3 axons

Top row: sequence of changes in i-dCA3 projecting CA3 axons. Training as well as the post-training Pr periods are characterized by a spatially selective addition of previously non-place-coding axons to the place map. These newly place-coding axons are preferentially active just before the aversive stimulus location. Additionally, during the Pr phase, a spatially unselective, pronounced stabilization of this spatial map is observed. At the same time, the fraction of place-coding axons increases, and the quality of spatial representation at the population level is enhanced. Bottom row: changes in commissurally projecting d-dCA3 axons are subtler. During training, place-coding axons in the pre-airpuff zone are more stable than elsewhere on the linear track. First zone is demarcated in bright blue.

The generation of an increased number of place-coding i-dCA3 axons in the pre-airpuff zone is in line with the hypothesis that it is advantageous to generate a robust signal that predicts imminent danger. It suggests a model in which the ventral hippocampus generates a danger signal that is then integrated into contextual or spatial information in the dorsal hippocampus. Indeed, behavioral experiments in animals with selective inactivation of either the ventral or dorsal hippocampus have shown that ventral and intermediate portions of the hippocampus are required for all types of fear memory, whether contextual or cued.[23–27] Conversely, dorsal lesions impair the formation of memories that require the association of affective and contextual information, whereas simpler cued fear memories are unaffected.[28] *De novo* generation of a danger signal could be used by downstream regions in the dorsal hippocampus to promote threat-related reconfiguration and plasticity of spatial maps. Indeed, in CA1, both spatial and rate remapping have been

observed following electric shock or aversive airpuff stimulation,[29–31] confrontation with a predatory robot,[32] or exposure to predator urine.[33,34] Importantly, in most of these instances, remapping is most pronounced at locations close to the aversive stimulus location. Of note, this danger-induced remapping in the dorsal CA1 was prevented by amygdala lesions,[32] underscoring the need for information transfer from the amygdala system to the dorsal hippocampus.

In parallel to the increased representation of the pre-airpuff zone, we observed an increasingly precise spatial representation by the i-dCA3 population during learning. In fact, the i-dCA3 axons eventually encode space equally well as the d-dCA3 axon population (see Figure 4). It has been previously shown that at the population level, the representation of space by ventral CA3 neurons can be comparable to dorsal hippocampus despite a lower number of place cells with larger place fields.[16] Our data now show that the population code for space in i-dCA3 axons is plastic

and becomes more precise during learning. It is possible that this information is also relevant for a more fine-scale spatial representation of dorsal CA1 neurons observed in an inhibitory avoidance task, in particular close to an aversive stimulus location.[35] We also found that i-dCA3 place axons are the main contributors to improved spatial coding even though they constitute a small minority of the entire axon population. This is likely due to the fact that in the i-dCA3 population, place axons are the most active, with most other axons being relatively quiescent during locomotion. This is unlike the dorsal hippocampal CA3 or CA1 neurons and might permit i-dCA3 axons to generate a sparse, low-noise danger signal. This signal could be further used to drive selection of salient stimuli in the dorsal CA3 region.[36]

Tracking the same axons across sessions allowed us to determine the underlying changes during learning at the level of single CA3 axons. In i-dCA3 projections, we found that there is a consistent appearance of newly place-coding axons within the pre-airpuff zone both during training and Pr intervals (see Figure 6). Following training, the stability of the place coding of i-dCA3 axons was strongly increased across all linear track locations. This suggests that newly place-coding axons give rise to a subsequently stabilized danger signal within the spatial map. It should be noted that the i-dCA3 system has a large number of non-place-coding axons, raising the possibility that these may constitute a reservoir of axons that are capable of generating multiple distinct danger codes if necessary. These learning-associated changes are fundamentally different from the threat-associated remapping seen in the dorsal CA1 region, in which mainly spatial and rate remapping have been observed or a migration of place fields toward the aversive location.[37]

We note that our behavioral paradigm does not allow us to discriminate which strategy mice use to determine the location of the aversive stimulation. They might learn the spatial location of the airpuff, but they might also use an egocentric strategy to determine the location of the aversive stimulus as a function of distance from another salient landmark like the reward site.

What form of plasticity could drive the recruitment of i-dCA3 neurons into spatial codes? In general, plasticity in the CA3 system is thought to contribute to storage of information within the CA3 network.[38] More specifically, artificially inducing plasticity between CA3 neurons encoding a fear memory and CA3 neurons encoding a neutral environment induces a fear association with the previously neutral environment,[39] supporting the view that plasticity in the CA3-CA3 system is used to associate contextual and affective information. Our data do not allow us to pinpoint the plasticity mechanism but reveal that those i-dCA3 cells that are destined to become place cells have significantly higher activity during locomotion than those cells that do not convert to place coding. This suggests a mechanism that triggers i-dCA3 cells to switch from a relatively silent to a more active state during locomotion, thus enabling them to more efficiently accumulate spatial information. Modulatory neurotransmitters such as acetylcholine are potential candidates for such a mechanism, as blocking mACh receptors blocks place field remapping during aversive learning[40] (for a review of a role of acetylcholine in remapping, see Dannenberg et al.[41]).

In summary, our results suggest that i-dCA3 axons exhibit a unique sequence of altered coding during aversive spatial learning that generates a precise, noise-poor, and stable danger signal that is available for integration with spatial and contextual information.

Limitations of the study

In summary, our results suggest that i-dCA3 axons exhibit a unique sequence of altered coding during aversive spatial learning that generates a precise, noise-poor, and stable danger signal that is available for integration with spatial and contextual information. We note that these results were obtained on a linear track with relevant stimuli arranged in limited 1D space. To see if these findings translate to a more naturalistic setting, it would be necessary to perform similar experiments using freely moving mice in larger environments.

STAR★METHODS

Detailed methods are provided in the online version of this paper and include the following:

- KEY RESOURCES TABLE
- RESOURCE AVAILABILITY
  - Lead contact
  - Materials availability
  - Data and code availability
- EXPERIMENTAL MODEL AND SUBJECT DETAILS
- METHOD DETAILS
  - Viral transduction and implantation of head fixation
  - Immunohistochemistry
  - Behavioral paradigm
  - Craniotomy and hippocampal window implantation
  - Two-photon calcium imaging
- QUANTIFICATION AND STATISTICAL ANALYSIS
  - Two-photon imaging
  - Generalized linear model, GLM
  - PCA
  - Place coding analysis and spatial tuning
  - Speed to place field correlation
  - Behavior

AUTHOR CONTRIBUTIONS

N.N. and H.B. conceived and planned the study. N.N. performed imaging experiments and data analysis. M.P. designed data analysis scripts and contributed strongly to data analysis. A.M.-L. and T.T. performed PCA-based data

REFERENCES

1. Moser, M.B., and Moser, E.I. (1998). Functional differentiation in the hippocampus. Hippocampus 8, 608–619. https://doi.org/10.1002/(SICI)1098-1063.

2. Kjelstrup, K.G., Tuvnes, F.A., Steffenach, H.-A., Murison, R., Moser, E.I., and Moser, M.-B. (2002). Reduced fear expression after lesions of the ventral hippocampus. Proc. Natl. Acad. Sci. USA 99, 10825–10830. https://doi.org/10.1073/pnas.152112399.

3. Henke, P.G. (1990). Hippocampal pathway to the amygdala and stress ulcer development. Brain Res. Bull. 25, 691–695. https://doi.org/10.1016/0361-9230(90)90044-z.

4. Gründemann, J., Bitterman, Y., Lu, T., Krabbe, S., Grewe, B.F., Schnitzer, M.J., and Lüthi, A. (2019). Amygdala ensembles encode behavioral states. Science 364, eaav8736. https://doi.org/10.1126/science.aav8736.

5. Pikkarainen, M., Rönkkö, S., Savander, V., Insausti, R., and Pitkänen, A. (1999). Projections from the lateral, basal, and accessory basal nuclei of the amygdala to the hippocampal formation in rat. J. Comp. Neurol. 403, 229–260.

6. Pitkänen, A., Pikkarainen, M., Nurminen, N., and Ylinen, A. (2000). Reciprocal connections between the amygdala and the hippocampal formation, perirhinal cortex, and postrhinal cortex in rat. Ann. N. Y. Acad. Sci. 911, 369–391. https://doi.org/10.1111/j.1749-6632.2000.tb06738.x.

7. Hintiryan, H., Bowman, I., Johnson, D.L., Korobkova, L., Zhu, M., Khanjani, N., Gou, L., Gao, L., Yamashita, S., Bienkowski, M.S., et al. (2021). Connectivity characterization of the mouse basolateral amygdalar complex. Nat. Commun. 12, 2859. https://doi.org/10.1038/s41467-021-22915-5.

8. Ishizuka, N., Weber, J., and Amaral, D.G. (1990). Organization of intrahippocampal projections originating from CA3 pyramidal cells in the rat. J. comp. Neurol. 295, 580–623.

9. Li, X.G., Somogyi, P., Ylinen, A., and Buzsáki, G. (1994). The hippocampal CA3 network: an in vivo intracellular labeling study. J. Comp. Neurol. 339, 181–208. https://doi.org/10.1002/cne.903390204.

10. Wittner, L., Henze, D.A., Záborszky, L., and Buzsáki, G. (2007). Three-dimensional reconstruction of the axon arbor of a CA3 pyramidal cell recorded and filled in vivo. Brain Struct. Funct. 212, 75–83. https://doi.org/10.1007/s00429-007-0148-y.

11. Swanson, L.W., Wyss, J.M., and Cowan, W.M. (1978). An autoradiographic study of the organization of intrahippocampal association pathways in the rat. J. comp. Neurol. 181, 681–715.

12. Amaral, D.G., and Witter, M.P. (1989). The three-dimensional organization of the hippocampal formation: A review of anatomical data. Neurosci 31, 571–591.

13. Steffenach, H.-A., Sloviter, R.S., Moser, E.I., and Moser, M.-B. (2002). Impaired retention of spatial memory after transection of longitudinally oriented axons of hippocampal CA3 pyramidal cells. Proc. Natl. Acad. Sci. USA 99, 3194–3198. https://doi.org/10.1073/pnas.042700999.

14. Royer, S., Sirota, A., Patel, J., and Buzsáki, G. (2010). Distinct representations and theta dynamics in dorsal and ventral hippocampus. J. Neurosci. 30, 1777–1787. https://doi.org/10.1523/JNEUROSCI.4681-09.2010.

15. Kjelstrup, K.B., Solstad, T., Brun, V.H., Hafting, T., Leutgeb, S., Witter, M.P., Moser, E.I., and Moser, M.-B. (2008). Finite scale of spatial representation in the hippocampus. Science 321, 140–143. https://doi.org/10.1126/science.1157086.

16. Keinath, A.T., Wang, M.E., Wann, E.G., Yuan, R.K., Dudman, J.T., and Muzzio, I.A. (2014). Precise spatial coding is preserved along the longitudinal hippocampal axis. Hippocampus 24, 1533–1548. https://doi.org/10.1002/hipo.22333.

17. Dombeck, D.A., Harvey, C.D., Tian, L., Looger, L.L., and Tank, D.W. (2010). Functional imaging of hippocampal place cells at cellular resolution during virtual navigation. Nat. Neurosci. 13, 1433–1440. https://doi.org/10.1038/nn.2648.

18. Danielson, N.B., Kaifosh, P., Zaremba, J.D., Lovett-Barron, M., Tsai, J., Denny, C.A., Balough, E.M., Goldberg, A.R., Drew, L.J., Hen, R., et al. (2016). Distinct Contribution of Adult-Born Hippocampal Granule Cells to Context Encoding. Neuron 90, 101–112. https://doi.org/10.1016/j.neuron.2016.02.019.

19. Landler, L., Ruxton, G.D., and Malkemper, E.P. (2019). The Hermans-Rasson test as a powerful alternative to the Rayleigh test for circular statistics in biology. BMC Ecol. 19, 30. https://doi.org/10.1186/s12898-019-0246-8.

20. Mizuta, K., Nakai, J., Hayashi, Y., and Sato, M. (2021). Multiple coordinated cellular dynamics mediate CA1 map plasticity. Hippocampus 31, 235–243. https://doi.org/10.1002/hipo.23300.

21. Bourboulou, R., Marti, G., Michon, F.-X., El Feghaly, E., Nouguier, M., Robbe, D., Koenig, J., and Epsztein, J. (2019). Dynamic control of hippocampal spatial coding resolution by local visual cues. Elife 8, e44487. https://doi.org/10.7554/eLife.44487.

22. Stefanini, F., Kushnir, L., Jimenez, J.C., Jennings, J.H., Woods, N.I., Stuber, G.D., Kheirbek, M.A., Hen, R., and Fusi, S. (2020). A Distributed Neural Code in the Dentate Gyrus and in CA1. Neuron 107, 703–716.e4. https://doi.org/10.1016/j.neuron.2020.05.022.

23. Rogers, J.L., Hunsaker, M.R., and Kesner, R.P. (2006). Effects of ventral and dorsal CA1 subregional lesions on trace fear conditioning. Neurobiol. Learn. Mem. 86, 72–81. https://doi.org/10.1016/j.nlm.2006.01.002.

24. Hunsaker, M.R., and Kesner, R.P. (2008). Dissociations across the dorsal-ventral axis of CA3 and CA1 for encoding and retrieval of contextual and auditory-cued fear. Neurobiol. Learn. Mem. 89, 61–69. https://doi.org/10.1016/j.nlm.2007.08.016.

25. Maren, S., and Holt, W.G. (2004). Hippocampus and Pavlovian fear conditioning in rats: muscimol infusions into the ventral, but not dorsal, hippocampus impair the acquisition of conditional freezing to an auditory conditional stimulus. Behav. Neurosci. 118, 97–110. https://doi.org/10.1037/0735-7044.118.1.97.

26. Rudy, J.W., and Matus-Amat, P. (2005). The ventral hippocampus supports a memory representation of context and contextual fear conditioning: implications for a unitary function of the hippocampus. Behav. Neurosci. 119, 154–163. https://doi.org/10.1037/0735-7044.119.1.154.

27. Wang, M.E., Fraize, N.P., Yin, L., Yuan, R.K., Petsagourakis, D., Wann, E.G., and Muzzio, I.A. (2013). Differential roles of the dorsal and ventral hippocampus in predator odor contextual fear conditioning. Hippocampus 23, 451–466. https://doi.org/10.1002/hipo.22105.

28. Kim, J.J., and Fanselow, M.S. (1992). Modality-specific retrograde amnesia of fear. Science 256, 675–677. https://doi.org/10.1126/science.1585183.

29. Wu, C.-T., Haggerty, D., Kemere, C., and Ji, D. (2017). Hippocampal awake replay in fear memory retrieval. Nat. Neurosci. 20, 571–580. https://doi.org/10.1038/nn.4507.

30. Moita, M.A.P., Rosis, S., Zhou, Y., LeDoux, J.E., and Blair, H.T. (2004). Putting fear in its place: remapping of hippocampal place cells during

fear conditioning. J. Neurosci. *24*, 7015–7023. https://doi.org/10.1523/JNEUROSCI.5492-03.2004.

31. Okada, S., Igata, H., Sasaki, T., and Ikegaya, Y. (2017). Spatial Representation of Hippocampal Place Cells in a T-Maze with an Aversive Stimulation. Front. Neural Circuits *11*, 101. https://doi.org/10.3389/fncir.2017.00101.

32. Kim, E.J., Park, M., Kong, M.-S., Park, S.G., Cho, J., and Kim, J.J. (2015). Alterations of hippocampal place cells in foraging rats facing a "predatory" threat. Curr. Biol. *25*, 1362–1367. https://doi.org/10.1016/j.cub.2015.03.048.

33. Wang, M.E., Wann, E.G., Yuan, R.K., Ramos Álvarez, M.M., Stead, S.M., and Muzzio, I.A. (2012). Long-term stabilization of place cell remapping produced by a fearful experience. J. Neurosci. *32*, 15802–15814. https://doi.org/10.1523/JNEUROSCI.0480-12.2012.

34. Wang, M.E., Yuan, R.K., Keinath, A.T., Ramos Álvarez, M.M., and Muzzio, I.A. (2015). Extinction of Learned Fear Induces Hippocampal Place Cell Remapping. J. Neurosci. *35*, 9122–9136. https://doi.org/10.1523/JNEUROSCI.4477-14.2015.

35. Schuette, P.J., Reis, F.M.C.V., Maesta-Pereira, S., Chakerian, M., Torossian, A., Blair, G.J., Wang, W., Blair, H.T., Fanselow, M.S., Kao, J.C., and Adhikari, A. (2020). Long-Term Characterization of Hippocampal Remapping during Contextual Fear Acquisition and Extinction. J. Neurosci. *40*, 8329–8342. https://doi.org/10.1523/JNEUROSCI.1022-20.2020.

36. Terada, S., Geiller, T., Liao, Z., O'Hare, J., Vancura, B., and Losonczy, A. (2022). Adaptive stimulus selection for consolidation in the hippocampus. Nature *601*, 240–244. https://doi.org/10.1371/journal.pcbi.1005423.

37. Mamad, O., Agayby, B., Stumpp, L., Reilly, R.B., and Tsanov, M. (2019). Extrafield Activity Shifts the Place Field Center of Mass to Encode Aversive Experience. eNeuro *6*. https://doi.org/10.1523/ENEURO.0423-17.2019.

38. Mishra, R.K., Kim, S., Guzman, S.J., and Jonas, P. (2016). Symmetric spike timing-dependent plasticity at CA3-CA3 synapses optimizes storage and recall in autoassociative networks. Nat. Commun. *7*, 11552. https://doi.org/10.1038/ncomms11552.

39. Oishi, N., Nomoto, M., Ohkawa, N., Saitoh, Y., Sano, Y., Tsujimura, S., Nishizono, H., Matsuo, M., Muramatsu, S.-I., and Inokuchi, K. (2019). Artificial association of memory events by optogenetic stimulation of hippocampal CA3 cell ensembles. Mol. Brain *12*, 2. https://doi.org/10.1186/s13041-018-0424-1.

40. Blair, G.J., Guo, C., Wang, S., Fanselow, M.S., Golshani, P., Aharoni, D., and Blair, H.T. (2023). Hippocampal place cell remapping occurs with memory storage of aversive experiences. Elife *12*, e80661. https://doi.org/10.7554/eLife.80661.

41. Dannenberg, H., Young, K., and Hasselmo, M. (2017). Modulation of Hippocampal Circuits by Muscarinic and Nicotinic Receptors. Front. Neural Circuits *11*, 102. https://doi.org/10.3389/fncir.2017.00102.

42. Pofahl, M., Nikbakht, N., Haubrich, A.N., Nguyen, T., Masala, N., Distler, F., Braganza, O., Macke, J.H., Ewell, L.A., Golcuk, K., and Beck, H. (2021). Synchronous activity patterns in the dentate gyrus during immobility. Elife *10*, e65786. https://doi.org/10.7554/eLife.65786.

43. Lovett-Barron, M., Kaifosh, P., Kheirbek, M.A., Danielson, N., Zaremba, J.D., Reardon, T.R., Turi, G.F., Hen, R., Zemelman, B.V., and Losonczy, A. (2014). Dendritic inhibition in the hippocampus supports fear learning. Science *343*, 857–863.

44. Greenberg, D.S., and Kerr, J.N.D. (2009). Automated correction of fast motion artifacts for two-photon imaging of awake animals. J. Neurosci. Methods *176*, 1–15. https://doi.org/10.1016/j.jneumeth.2008.08.020.

45. Pnevmatikakis, E.A., Soudry, D., Gao, Y., Machado, T.A., Merel, J., Pfau, D., Reardon, T., Mu, Y., Lacefield, C., Yang, W., et al. (2016). Simultaneous Denoising, Deconvolution, and Demixing of Calcium Imaging Data. Neuron *89*, 285–299. https://doi.org/10.1016/j.neuron.2015.11.037.

46. Glaser, J.I., Benjamin, A.S., Chowdhury, R.H., Perich, M.G., Miller, L.E., and Kording, K.P. (2020). Machine learning for neural decoding. eNeuro *7*. https://doi.org/10.1523/ENEURO.0506-19.2020.

47. Kay, K., Sosa, M., Chung, J.E., Karlsson, M.P., Larkin, M.C., and Frank, L.M. (2016). A hippocampal network for spatial coding during immobility and sleep. Nature *531*, 185–190. https://doi.org/10.1038/nature17144.

48. Duda, R.O., and Hart, P.E. (1972). Use of the Hough transformation to detect lines and curves in pictures. Commun. ACM *15*, 11–15. https://doi.org/10.1145/361237.361242.

STAR★METHODS

KEY RESOURCES TABLE

REAGENT or RESOURCE	SOURCE	IDENTIFIER
Antibodies		
STEP2	Cell Signaling	Cat# 4396; RRID:AB_1904101
Anti-Dynorphin	Abcam	Cat# ab82509, RRID:AB_2049593
T-4102 Rabbit anti-Somatostatin-14 IgG	BMA BIOMEDICALS	Cat# A19PO22037
Bacterial and virus strains		
pAAV.Syn.Flex.GCaMP6s.WPRE.SV40	Addgene	Plasmid #100845; RRID:Addgene_100845
Experimental models: Organisms/strains		
B6(129S)-Et(icre)21614Rdav/Mmmh	Mmrrcc	034580-MU; RRID:MMRRC_034580-MU
Software and algorithms		
MATLAB (Natick, MA: The Math Works, Inc., 2020)	Math Works, Inc.	Version R2020b

RESOURCE AVAILABILITY

Lead contact
Further information and requests for resources and reagents should be directed to and will be fulfilled by the lead contact, Heinz Beck (Heinz.beck@ukbonn.de).

Materials availability
This study did not generate new unique reagents.

Data and code availability
- The codes are made available on the following GitHub repository: https://doi.org/10.5281/zenodo.10576417.
- Data is available on Dryad, named "CA3 axonal calcium imaging": https://doi.org/10.5061/dryad.stqjq2c72.
- Any additional information required to reanalyze the data reported in this work paper is available from the lead contact upon request.

EXPERIMENTAL MODEL AND SUBJECT DETAILS

In these experiments, we used 6–12 weeks old Et-iCre transgenic mice generated by Ronald L. Davis and Paul Overbeek (B6(129S)-Et(icre)21614Rdav/Mmmh, CRE-driver network established by the NIH Neuroscience Blueprint).For animal studies with *in-utero* electroporation, timed pregnant mice were used at embryonic day 14 (E14). Male C57Bl/6 and female CD1 mice were allowed to mate overnight (Obtained from Charles River).

All animal experiments were conducted in accordance with European (2010/63/EU) and federal law (TierSchG, TierSchVersV) on animal care and use and approved by the county of North-Rhine Westphalia (LANUV AZ 84-02.04. 2015.A524). Animals were single caged or in rare occasions kept in cages of maximum two mice. They were maintained on a 12-h light/dark cycle (lights on from 6 p.m. until 6 a.m.). Behavioral training and testing was done during the dark phase. They had access to *ad libitum* amount of food before the start of the actual experiments. In this study we used 6–12 weeks old Et-iCre transgenic mice generated by Ronald L. Davis and Paul Overbeek (B6(129S)-Et(icre)21614Rdav/Mmmh, CRE-driver network established by the NIH Neuroscience Blueprint).

METHOD DETAILS

Viral transduction and implantation of head fixation
In a single operation injection of virus leading to Cre-dependent expression of GCaMP6s (pAAV.Syn.Flex.GCaMP6s.WPRE.SV40, AAV1) and implantation of a customized head fixation was performed.[42] The animals were subcutaneously (s.c.) injected with ketoprofen (5 mg/kg body weight) 30 min prior to the surgery. They were then anesthetized with a combination of fentanyl/midazolam/medetomidine (0.05/5.0/0.5 mg/kg body weight i.p.) and were head-fixed in a stereotactic frame. Their body temperature was kept on a heat-plate at 37°C and their eye were covered with eye ointment (Bepanthen, Bayer) in order to prevent them from drying out. The hair over the scalp was cut short and then was cleared completely with a hair-remover cream. The scalp was then completely disinfected. After the application of local anesthetic (10% lidocaine), a pear-like circumference of skin was removed.

Lidocaine was reapplied and the thin transparent remaining tissue under the scalp was removed with a scalpel. With a dental drill a golf-ball pattern all over the skull was generated in order to increase the adhesion of dental cement. The skull was then cleaned further with a Q-tip immersed in 1% H_2O_2 and rinsed with 2mL phosphate buffered saline. After drying, a thin layer of the primary component of OptiBond (OptiBond3FL; two components, 48 filled dental adhesive, bottle kit; Kerr; FL, USA) was applied. The secondary component of OptiBond was then applied and cured with a UV lamp. Subsequently, a small craniotomy for virus injection was made using a dental drill with the following coordinates: Dorsal CA3: AP: −0.1; LA: +0.1; VD: −0.17 (see Figure 1; Figure S1 and Videos S1 and S3) and ventral CA3: AP: −0.3; LA: −0.32; VD: −0.37 (see Figure 1; Figure S1 and Videos S2 and S4). Subsequently, the tip of NanoFil Microsyringe (NANOFIL, 10μL, cannula size 34 G, World Precision Instruments, Sarasota, FL) was navigated stereotactically through the burrhole to the target position. For dorsal CA3, 250 nL of virus particle suspension was injected, for ventral CA3, 300 nL of virus particle suspension was used (injection speed 20 nL/min). The position of the cranial window was marked using a 3mm biopsy punch (Kai Medical, IntegraMiltex disposable biopsy punch 3mm). To have a stable fluorescent signal for motion correction, a virus leading to expression of mCherry under a GFAP promoter was injected at the position of the crainal window (rAAV 2/1- GFAP-mCherry). Specifically, these injections were done in 3 different locations within the imaging window, and at each location in two different depths to ensure widespread mCherry expression for motion correction (1st injection: AP: −0.14; LA: −0.1; VD: −0.14, −0.17, 2nd injection: AP: −0.3; LA: −0.32; VD: −0.37, 3rd injection: AP: −0.3; LA: −0.32; VD: −0.37). A total volume of 150 nL was used during each injection (speed 20 nL/min). The injection holes were covered with a thin layer of UV-curing dental cement (Tetric Evoflow). At this point Tetric Evoflow was applied in a circular fashion close to the marginal skin. A small amount of dental cement was applied underneath the head fixation. The head fixation was then placed on the skull and UV-cured. Antibiotic ointment was applied to the skin surrounding the head fixation and naloxon was injected i.p. (0.1 mL/10 gr body weight). Mice were then returned to their cages. The cages were kept on a heating pad for few days after the surgery and a small amount of soaked food was placed on the floor of the cage for easy access. Postoperative buprenorphine was given once daily for 3 days following the surgery (5 mg/kg body weight, s.c.).

Immunohistochemistry

For immunohistochemistry, the brains of Et-iCre-td-tomato were sliced in 70 μm slices with a vibratome (Leica). They were washed and stored in 4% PFA for 24 h and then washed in PBS 3x5 minutes. For STEP2 staining, the slices were incubated in the blocking buffer (phosphate buffered saline, PBS with 5% normal serum and 0.3% Triton X-100) and were then incubated with the STEP2 antibody (Cell Signaling Technology #4396, 1:100) overnight at 4°C. The next day the slices were rinsed 3 times with 1xPBS and incubated in immune-conjugated antibody in dark for 2 h in room temperature (RT). The same slices were taken for the Dynorphin staining. A heat antigen retrieval procedure was performed for which the slices were washed 3 × 5 min in PBS with gentle agitation. They were then incubated in 10 mM nacitrate (pH = 8.5) preheated to 80°C (in Eppendorf tubes in Thermomixer), and afterward stored in 1 mL sodium citrate für 20 min, then cooled down to RT in sodium citrate followed by 3 × 5 minutes wash in PBS. The blocking procedure was conducted as for the STEP2 procedure, washed for 3 × 5 minutes with PBS and incubated in the anti-Dynorphin antibody diluted in Brodey buffer over night at 4°C. After washing 3 × 5 min in 1mL PBS, secondary antibody Cy3/5 (1:400) diluted in Bordey buffer was put on the slices for 2 h in RT. Finally, they were washed 3 × 5min in 1 mL PBS. After the *in vivo* experiments, the brains were extracted and stored in 4% PFA for at least 24hrs. They were then rinsed off PFA with PBS (3x rinse) and sliced with a to 70 μm coronal slices. For nuclear staining, brain slices were kept for 10 min in DAPI solution (1:1000) at RT. Brain slices were mounted and the red, green and blue fluorescent channels were successively imaged using an Epi-fluorescent or spinning-disc microscope (Visitron VisiScope).

Behavioral paradigm

The behavioral paradigm used in this project was a modified version of con-text-dependent fear conditioning as described in,[43] adapted to our two-photon setup and head-fixed condition. After a week of recovery following the virus injection and head-fixation implantation, the animals were habituated to the horizontal treadmill and the head-fixed condition running on the belt according to the following protocol. On the first day after recovery, mice were allowed to freely explore the treadmill. During this day, mice were placed two or three times during the active phase on the apparatus to sniff around and freely explore the environment and the belt, each time for maximum of 10 min. On consecutive days, habituation to the head fixation was carried out. Mice were head fixed on the setup on each day for 2 × 10 min, until all signs of anxiety subsided and mice ran freely on the linear treadmill, with a plain belt. Such habituation days were repeated until the animals reached a steady performance and completed a minimum of 10 rounds in 20 min, up to two weeks after virus injection/head fixation implantation. Simultaneously with the habituation session, starting one week after the surgery, *ad libitum* food was discontinued and a scheduled food diet according to our animal-grant (AZ 84-02.04. 2014.A254) was administered. The protocol was as follows: On the first two days of the food scheduling protocol, the animals received a measured amount of food. On the evening of the second day the remaining food was weighed in order to define the consumed amount of food. This value was divided by 2 and the corresponding amount of 1 gr food pellets (Dustless Precision PelletsRodent, Grain-Based, BioServe) were placed onto the cage floor for consumption. The weight of mice and the consumed amount of food was supervised every day until they reached to almost 85% of their initial body mass. Additional care was taken in order to make this adjustment according

to the general health and behavior status of each animal. During the food scheduling period, a heat-pad was placed underneath the cage to keep mice warm. During the habituation and behavioral sessions on the linear track, the animals received liquid food rewards at the end of each lap (diluted Butler Supplical Pet Multi-vitamin).

Once the habituation phase was completed, cranial window implantation was carried out, followed by a recovery period. After recovery, we initiated the baseline and aversive learning protocol.

On each of the first two days of the protocol, two 20-min baseline sessions were carried out (session start of the second session 60–90 min after the first) on a new, cue-enriched linear track. The first session on the first day was discarded as the mice were confronted with the cue enriched linear track for the first time. The last three baseline sessions before inception of training sessions were consistently termed B_1-B_3. During these sessions, all animals ran at least 8 laps during each 20 min session with an average of 21 laps per session.

On the next days of the protocol, twice daily 20-min training sessions were carried out, also 60–90 min apart. Two daily training sessions proved ideal to allow mice to learn the location of the relatively mild aversive stimulation. During training sessions, animals received a puff of compressed air each time they passed the border of the first and the second zones on the belt (at 50 cm according to the convention in all figures). Training sessions were repeated for as many days as needed until the animals showed apparent slowing down or stopping behavior close to the airpuff location. Following the last training session, on the next day, a probe session was carried out. During the probe session, no airpuff was applied to test if slowing at the previous airpuff location persists, indicating memory formation. Thus, equal, ~24 h time intervals were present between sessions B_1-B_2, B_3-T_1, T_n-Pr, these equal time intervals were used to quantitatively compare dynamics of place coding over time.

Speed on the linear track was analyzed with custom written code in Python. First, we binned the speeds for every 1 cm on the belt, and added the binned data to a matrix with a dimension of "number of rounds x number of bins". Color coded speed maps made consistent slowing readily visible during training (see Figure S2, for more details on the statistical analysis of running behavior see STAR Methods section data analysis, behavior below).

Craniotomy and hippocampal window implantation

45 min before the start of the surgery dexamethasone was i.p. injected (0.1mg/20 g body weight) in order to inhibit brain inflammation during surgery. The animal was anesthetized inside an induction chamber with 3–4% isoflurane mixed with an oxygen/air mixture (25/75%) and was then transferred to a stereotactic frame. An isoflurane mask was put on the snout and the head was fixed using head-bars. The anesthesia was maintained with a reduced isoflurane dose of 1–2% at a gas flow of about 0.5 L/min. Eyes were covered with eye-ointment (Bepanthen, Bayer) to prevent drying and body temperature was maintained at 37°C using a regulated heating plate (TCAT-2LV, Physitemp). The skull in the middle of head-ring was thoroughly cleaned using a Q-tip soaked in 70% ethanol. A Ø 3 mm craniotomy was made using a dental drill. The circular piece of skull was gently removed and any remaining bones around the edges were smoothed and drilled away. The cortex was then carefully aspirated with a blunt 27-gauge needle attached to a suction system until the alveus of the hippocampus became visible. When required, irrigation with dPBS was carried out to avoid blood clotting and brain drying.

Two-photon calcium imaging

We used a commercially available two photon microscope (A1 MP, Nikon) equipped with a 16x long-working-distance, water-immersion objective (N.A. = 0.8, WD = 3 mm, CFI75 LWD 16X W, Nikon) controlled by NIS-Elements software (Nikon). GCaMP6s was excited at 920 nm using a Ti:Sapphire laser system (~60 fs laser pulse width; Chameleon Vision-S, Coherent). Emitted photons were collected using gated GaAsP photomultipliers (H11706-40, Hamamatsu). Movies were recorded using a resonant scanning system at a frame rate of 15 Hz and duration of 20 min per movie.

QUANTIFICATION AND STATISTICAL ANALYSIS

Two-photon imaging

All analysis on imaging data and treadmill behavior data were conducted in MATLAB and Python using standard toolboxes, open access toolboxes and custom written code. To remove motion artifacts, recorded movies were registered using a Lucas–Kanade model.[44] Individual cell locations and fluorescence traces were identified using a constrained nonnegative matrix factorization based algorithm and afterward Ca^{2+} events were identified with a constrained deconvolution algorithm.[45] In order to overcome the issues of segmentation of axonal branches into smaller components an iterative merging approach was implemented. This approach was based on the correlation of the spatial footprints as well as to the temporal correlation of calcium traces of identified axons. After component extraction, those components with spatial and temporal correlations above Pearsons' r > 0.2 were carefully compared individually. After inspection, components or sub-branches belonging to the same axons were merged by adding those components to each other.

In order to follow axons over days, a 2D cross-correlation approach was utilized using standard MATLAB image registration procedures. To align the FOV between days, the astrocytic label in the red channel was used to create a rigid 2D transformation. This transformation was applied to the spatial footprints of all components. The components in the green GCaMP6s channel were then matched using the spatial footprints of each day and calculating the components with the highest 2D cross-correlation values, where

maximum shift of 10 pixels was allowed between the reference and the current component. The components were assigned hierarchically and the components with r < 0.2 were rejected. All identified matches were inspected visually and false positive matches were rejected.

Generalized linear model, GLM

to fit a generalized linear model to the imaging data we used standard MATLAB procedures. We assigned an angle to each position on the belt and split the data in a *sin* and *cos* – component to generate to continuous variables in order to fit the data to the mouse position. The first 16 min of each session were used for fitting and the last 4 min (20%) were used to test the GLM. The accuracy of the model was estimated by calculating the standard deviation of the difference between calculated and real position of the animal during running periods.

PCA

Analysis was performed in Python using the numpy, scipy, scikit-learn, and matplotlib libraries. For the Principal Component (PCA) analysis, we chose at every session as many dimensions as needed to explain 90% of the variance. Position prediction was done by adapting the algorithms from,[46] available at https://github.com/KordingLab/Neural_Decoding, using the Extreme Gradient Boost algorithms. Shuffle data was created by shifting the neuronal activity in random increments, wrapping around the endpoints. For the place cell dropout experiments, first we determined at every session which type of cell (place or non-place) there was the least amount of, and then compared the prediction error of those cells with random combinations of the same number of cells of the opposite type.

Place coding analysis and spatial tuning

For the analysis of place related activity within CA3 projections we restricted analysis to running epochs, where a running epoch was defined as an episode of movement with a minimal duration of 2.5 s above a threshold of 4 cm/s in a forward direction. The threshold of 4 cm/s was chosen in line with both literature using head-fixed mice (i.e.,[18]), as well as a very extensive literature in freely moving animals (i.e.,[47]). Only the onset times of significant Ca^{2+}-transients were used in a binarized manner for the analysis and only components with 4 or more event onsets during running epochs were included in the analysis. To identify place coding components, we used criteria as described by.[17] Components that showed activity at a certain location on the belt in at least 20% of rounds and an average activity that was at least 7 times higher as in the rest of the belt were considered possible candidates. To access significance, the onsets of an individual component were randomly shuffled in time 1000 times. The p value for each cell was calculated as the percentage when the randomized activity matched the criteria as a place coding component. To assess the precision of spatial tuning in each significantly place coding component, we used spatial tuning vector analysis.[18] To that end we assigned angles to 1 cm bins all around the belt. To estimate the tuning vector calculated the mean of all angles were significant running related Ca^{2+}-event onsets occurred, weighted by the time spent in the respective bin. We used binarized data to calculate the mean of the vectors pointing in the mouse position at the times of transient onsets, weighted by the time spent in that bin. The tuning vector calculation requires that axons have single place fields, since the mean could otherwise lie between place fields. All significantly place coding axons in our data from both projections had only single place fields.

Speed to place field correlation

In order to correlate running speed to how densely a certain location is represented in the place code we calculated a place field density. This place field density was calculated for each animal and session as the mean of all significant place field maps of the respective session, where a bin size of 5 cm was used. The resulting vector is a direct measure for the density of individual place fields at each location on the belt. Correlations to running speed were calculated using Pearsons' r between the place field density and the mean running speed of the same session at a given location on the linear track.

Behavior

Even though consistent slowing was apparent in the speed maps for individual sessions following learning, reductions in speed before airpuff locations occurred at slightly variable locations, making simple averaging approaches less sensitive.

For calculation of brief speed reductions, the input speed data with a resolution of speed per 10 mm location bins were averaged over a moving window with 10 data points for each round on the belt. The averaged speeds were then z-scored and the data points below one standard deviations were highlighted. Episodes dipping below one standard deviation were then accumulating across the session. We then calculated how many of these minima occurred in the pre-airpuff zone (0–50 cm in our convention), normalized to the total number of minima across the linear track, with 33% indicating equal distribution of slowing episodes. Significance was evaluated by repeated measure ANOVA for the last baseline, last training and probe sessions.

We also developed a graphical method from computer vision to detect consistent slowing across laps. Speed data was converted to grayscale speed maps and binarized, using the 85th percentile as a threshold for the binarization. Using a robust feature extraction algorithm used in computer vision and image analysis (Hough transform,[48]) we detected vertical lines indicating consistent slowing. Hough transform uses parameter space for shape detection and utilizes an accumulator to hold values of the parameters, with the output being the most probable location of consistent slowing. Stops related to the reward acquisition were excluded. To test if

consistent slowing in the airpuff zone (defined as a zone of 20 cm, 10 cm on each side of the airpuff location) is by chance, we used null hypothesis significance testing. To generate the null distribution, we drew 10^7 samples of n line locations (with n equaling the experimentally obtained numbers) from a uniform distribution of integers ranging from 10 to 140 cm (representing the linear track, and excluding the reward zone). The random selection process also allowed duplicate values to exist. The probability of having n or higher number of lines in the AP zone, is defined as $\frac{N_{n+}}{N_m}$, where N_{n+} is the count of samples with n to m lines in the AP zone, and N_m is the total count of samples, in our case 10^7.